JACS
JOURNAL OF THE AMERICAN CHEMICAL SOCIETY
Article
pubs.acs.org/JACS

Dense CO Adlayers as Enablers of CO Hydrogenation Turnovers on Ru Surfaces

Jianwei Liu,[†,‡] David Hibbitts,[*,‡,§] and Enrique Iglesia[*,‡]

[†]State Key Laboratory of Heavy Oil Processing, China University of Petroleum, Qingdao 266580, China
[‡]Department of Chemical and Biomolecular Engineering, University of California, Berkeley, California 94720, United States
[§]Department of Chemical Engineering, University of Florida, Gainesville, Florida 32611, United States

Supporting Information

ABSTRACT: High CO* coverages lead to rates much higher than Langmuirian treatments predict because co-adsorbate interactions destabilize relevant transition states less than their bound precursors. This is shown here by kinetic and spectroscopic data—interpreted by rate equations modified for thermodynamically nonideal surfaces—and by DFT treatments of CO-covered Ru clusters and lattice models that mimic adlayer densification. At conditions (0.01−1 kPa CO; 500−600 K) which create low CO* coverages (0.3−0.8 ML from in situ infrared spectra), turnover rates are accurately described by Langmuirian models. Infrared bands indicate that adlayers nearly saturate and then gradually densify as pressure increases above 1 kPa CO, and rates become increasingly larger than those predicted from Langmuir treatments (15-fold at 25 kPa and 70-fold at 1 MPa CO). These strong rate enhancements are described here by adapting formalisms for reactions in nonideal and nearly incompressible media (liquids, ultrahigh-pressure gases) to handle the strong co-adsorbate interactions within the nearly incompressible CO* adlayer. These approaches show that rates are enhanced by densifying CO* adlayers because CO hydrogenation has a negative activation area (calculated by DFT), analogous to how increasing pressure enhances rates for liquid-phase reactions with negative activation volumes. Without these co-adsorbate effects and the negative activation area of CO activation, Fischer−Tropsch synthesis would not occur at practical rates. These findings and conceptual frameworks accurately treat dense surface adlayers and are relevant in the general treatment of surface catalysis as it is typically practiced at conditions leading to saturation coverages of reactants or products.

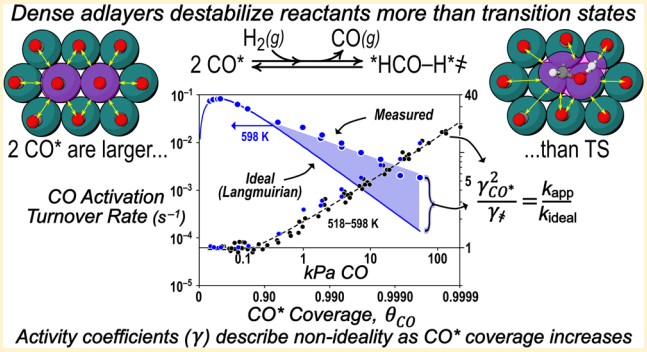

1. INTRODUCTION

Chemisorbed species on supported metal clusters alter the binding properties of co-adsorbed intermediates and transition states through a combination of "through-space" and "through-surface" interactions that affect reactivity, which cannot be rigorously described using Langmuirian treatments of surface catalysis.[1−13] O_2 dissociation, for instance, is essentially barrierless on sparsely covered Pt surfaces, and CO oxidation turnover rates on nearly bare surfaces are limited by the reaction of chemisorbed CO (CO*) with the O* atoms formed via O_2 dissociation.[1−3] At low coverages typical at high temperatures (>700 K), O* reactivity is controlled by the coordination of surface atoms to which O* is bound, and Langmuirian ensembles of sites with different coordination provide accurate, albeit empirical, descriptions of the effects of O* coverage and surface coordination on turnover rates.[3−5] Surfaces, however, form saturated dense CO* monolayers during CO oxidation at conditions relevant to its catalytic practice (400−600 K).[1−3,6,7] In such cases, direct O_2 dissociation requires a very high activation barrier, and the O═O bond is cleaved instead via bimolecular reactions of O_2* with CO*. Both CO* and O_2* are less stable, and thus more reactive within dense adlayers than on sparsely covered surfaces.[3,6] Strong co-adsorbate interactions weaken metal−adsorbate bonds, which then dampen the effects of surface coordination on the binding and reactive properties of relevant intermediates at high CO* coverages.[1−7] Consequently, surface atom coordination and metal cluster size effects on reactivity are much weaker within crowded adlayers than on nearly bare surfaces, the latter of which are consistently used by theoretical treatments of catalyst surfaces.

The diversity of reaction paths conferred by changes in adlayer density and the effects of coordination for CO oxidation reactions on saturated or sparsely covered surfaces[1−8] are also evident as O* coverages change during CH_4-O_2[9] and NO-O_2[10] reactions and also as CO* coverages change during alkanol decarbonylation[11] and CO hydrogenation[12,13] catalysis. In all cases, higher coverages cause the lateral compression of surface adlayers and the weakening of the bonds between adsorbed

Received: May 8, 2017
Published: August 21, 2017

DOI: 10.1021/jacs.7b04606
J. Am. Chem. Soc. 2017, 139, 11789−11802

species and surface atoms, thus increasing the reactivity of bound species and allowing their occasional desorption to create vacant sites required to adsorb co-reactants or dissociate species. Taken together, these coverage effects lead to higher rates on surfaces for which strongly bound species or strongly binding atoms of low coordination would inhibit turnovers.

Coverage effects of this type have been previously considered through modified microkinetic models[13−19] and by kinetic Monte Carlo methods[20−26] that implicitly or explicitly account for co-adsorbate interactions. Here, we will instead account for these co-adsorbate interactions by treating dense adlayers of adsorbates as thermodynamically nonideal systems for which the rates of surface reactions depend on their "areas of activation", through an analogy with the activation volumes often used for homogeneous reactions in dense and nonideal liquid and gaseous media.[27−33] Specifically, we address the effects of dense CO* adlayers and assess the adequacy of Langmuirian models for CO hydrogenation on Ru-based catalysts,[13,34−41] widely used along with Ni,[41−43] Co,[12,44−49] and Fe[47−51] catalysts, in methanation and Fischer−Tropsch synthesis (FTS). High CO pressures (>100 kPa) shift reaction selectivities from CH_4 products to larger hydrocarbons and lead to very dense saturated CO adlayers at all relevant conditions (450−550 K, 0.1−5 MPa). Such dense CO* adlayers are evident from kinetic and isotopic data,[35,36,44,47,48] infrared spectra,[37,38] and theoretical treatments.[38−40] Here, we show that such dense CO* adlayers prevail even at the higher temperatures (500−600 K) and lower CO pressures (0.1−100 kPa CO) typical of methanation conditions. Turnover rates of CO hydrogenation increase with particle size on both Co and Ru catalysts, indicating that low-index terraces of supported particles are the active sites for CO* activation.[45,52−56] On densely populated surfaces, and even on bare surfaces, the direct dissociation of strong C≡O bonds occurs through elementary steps with high activation barriers, which preclude them from occurring at detectable turnover rates. Defect sites attributed to direct CO* dissociation events when examined at low coverages[57−59] are inactive at high coverages[38,60] because of the inability to form the required vacancies in the presence of strongly bound CO*. H_2 linearly increases the rate of CO hydrogenation and does so by H* assisting the kinetically relevant CO* activation step, which weakens C≡O bonds via the formation of *HCOH* intermediates.[38,48,49,54,60−65] These species dissociate to form *OH and *CH species, which then form H_2O, CH_4, as well as the adsorbed monomers and chain initiators required to form C−C bonds and to grow hydrocarbon chains.

This H-assisted CO* activation mechanism[38,48,49,54,60−65] leads to rate equations based on Langmuirian models:

$$r_{CO} = \frac{\alpha P_{H_2} P_{CO}}{(1 + K_{CO} P_{CO})^2} \quad (1)$$

which adequately describe rate data on Fe,[48,49] Co,[48,49] Ni,[43] Ru,[35,38,40,60,65] and Rh[61] catalysts. In eq 1, K_{CO} is the equilibrium constant for the binding of molecular CO, and α is a lumped rate constant, which is determined by the free energy difference between the transition state for *HCOH* formation ($[*HCO-H*]^{\ddagger}$) and its gaseous CO and H_2 reagents. The overarching tenet of Langmuirian kinetic models states that the binding properties and the stability of all intermediates and transition states are independent of the coverage or the identity of any co-adsorbed spectator species, therefore, K_{CO} and α should be constant in Langmuir models. The K_{CO} values regressed from rate data on these catalysts indicate that CO* coverages would remain below saturation levels even at the high CO pressures (>100 kPa) and low temperatures (<500 K) required for chain growth in FTS reactions. Theoretical treatments[38−40] and infrared spectra[37,38] at these conditions, however, show that CO* species are present at saturation coverages, even at much lower CO pressures and significantly higher temperatures than those typical of FTS catalysis, a contradiction that has remained unresolved and essentially ignored in literature.

These inconsistencies reflect the inadequacy of Langmuirian models as descriptions of chemical dynamics in dense adlayers, despite their serendipitous ability to describe rate data over typically narrow reactant pressure ranges. Here, we consider the consequences of high CO* coverages for CO hydrogenation turnover rates by measuring rate data and infrared spectra during CO-H_2 reactions on Ru (7.5 nm) over a very broad CO pressure range (10^{-3}−10^2 kPa), which leads to CO* coverages spanning a range from nearly isolated CO* species to very dense CO* adlayers. Langmuirian models accurately describe CO* coverages only at submonolayer coverages (0.3−0.9 ML), and CO adsorption equilibrium constants (K_{CO}) from infrared spectra and kinetic analysis (using eq 1) agree well. Higher CO pressures lead to CO* infrared bands of nearly constant intensity, but with frequencies that increase monotonically with CO pressure and with CO* coverage, an indication that the densification of CO* adlayers causes a concomitant increase in intermolecular repulsion. At these higher CO pressures, hydrogenation turnover rates are much higher than predicted from the α and K_{CO} parameters derived from rate data at lower CO pressures using eq 1. These rate enhancements on surfaces nearly saturated with CO* are described here using transition-state theory formalisms appropriate for thermodynamically nonideal systems. Nonideality, in this context, describes a catalyst surface on which co-adsorbed species interact to an extent that causes their binding and reactive properties to vary with coverage, thus precluding accurate descriptions using Langmuirian models. The enhancements reflect a reaction whose transition state ($[*HCO-H*]^{\ddagger}$) is less destabilized by CO* adlayer densification than the two CO* it replaces because of its negative "activation area", analogous to the concept of activation volume used to describe pressure effects for homogeneous reactions in the liquid phase.[27−33] As a result, dense CO* adlayers lead to lower activation free energies, as confirmed here from theoretical treatments and lattice models. In doing so, these dense CO* adlayers lead to practical turnover rates at the conditions required for efficient chain growth in the Fischer−Tropsch synthesis on Ru catalysts[40,65] and, as our ancillary results indicate, also on Co-based catalysts.[46] This thermodynamic formalism is appropriate for descriptions of chemical reaction dynamics on densely covered surfaces using activities instead of concentration in the rate equation and describes the effects of CO pressure (and CO* coverage) on rates and infrared spectra; it is also consistent with the theoretical treatments reported here. This thermodynamic formalism accounts for co-adsorbate interactions in the context of nonideal thermodynamic treatments of reactivity over the entire range of surface coverages that prevail in the practice of CO hydrogenation.[35−40,48,49,61] Such descriptions also provide fundamental insights into the dynamics of the many other reactions that occur on nearly saturated surfaces, such as CO oxidation,[1−8] NO reduction,[66−69] C−C, or C−O

DOI: 10.1021/jacs.7b04606
J. Am. Chem. Soc. 2017, 139, 11789−11802

hydrogenolysis,[11,19,70] and oxygen reduction at electrode surfaces.[71−73]

2. METHODS

2.1. Catalysts Synthesis Procedures. SiO_2 (Davisil grade 62; 75−109 μm; 340 m^2 g^{-1}) was treated in flowing dry air (Praxair, 99.999%, 0.33 cm^3 s^{-1} g^{-1}) by heating to 1073 at 0.083 K s^{-1} and holding for 5 h. Ru was then dispersed on this SiO_2 using incipient wetness impregnation methods (5% wt. Ru). The impregnating solution contained $Ru(NO)(NO_3)_3$ (Alfa-Aesar, 32% wt. Ru) and triethanolamine (TEA; Sigma-Aldrich, 97%) (1:10 Ru:TEA molal ratio) in deionized H_2O (17.9 MΩ resistivity).[74] After impregnation, powders were treated sequentially (i) in stagnant ambient air by heating to 373 at 0.017 K s^{-1} and holding for 8 h; (ii) in flowing dry air (Praxair, 99.999%, 0.83 cm^3 s^{-1} g^{-1}) by heating to 673 at 0.033 K s^{-1} and holding for 3 h before cooling to ambient temperature; (iii) in 10% H_2/He (Praxair, 99.999%, 0.83 cm^3 s^{-1} g^{-1}) by heating to 723 at 0.033 K s^{-1} and holding for 3 h before cooling to ambient temperature in flowing He (Praxair, 99.999%, 0.83 cm^3 s^{-1} g^{-1}); and (iv) in 1% O_2/He (Praxair, 99.999%, 0.83 cm^3 $s^{-1}g^{-1}$) flow at ambient temperature for 1 h before exposure to ambient air.

2.2. Textural and Chemical Characterization Methods. Ru dispersion, defined as the fraction of atoms exposed at Ru particle surfaces, was measured from total volumetric H_2 uptakes at 3−50 kPa H_2 and 373 K.[75,76] Samples were held within a quartz cell and treated in flowing H_2 (Praxair, 99.999%, 0.2 cm^3 s^{-1} g^{-1}) by heating to 723 at 0.033 K s^{-1} and holding for 1 h; samples were then evacuated at 723 K for 1 h and cooled to 373 K under dynamic vacuum (0.73 Pa). H_2 uptakes were determined by extrapolation of the linear portion of isotherms to zero H_2 pressure,[75] and the number of exposed Ru atoms (Ru_{surf}) was calculated using a 1:1 H:Ru_{surf} stoichiometry.[76−78] Mean Ru particle diameters ($<d_{chem}>$ = 7.5 nm) were determined from chemisorption-derived dispersion values by assuming hemispherical crystallites and the atomic density of bulk Ru metal.[5,79]

Ru cluster size distributions (of >500 particles) were determined by transmission electron microscopy (TEM, Philips/FEI Tecnai 12). Surface-averaged diameters ($<d_{TEM}>$)[80] were calculated from

$$<d_{TEM}> = \frac{\sum n_i d_i^3}{\sum n_i d_i^2} \quad (2)$$

where n_i is the number of metal clusters with diameter d_i. A representative TEM image and a Ru particle size distribution are shown in Figure 1. The mean Ru diameter from TEM ($<d_{TEM}>$) was

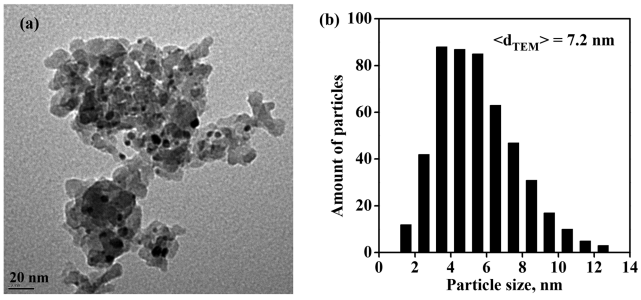

Figure 1. (a) TEM image and (b) Ru particle size distribution for 5% wt. Ru/SiO_2 catalyst.

7.2 nm, which is in agreement with H_2 chemisorption values ($<d_{chem}>$, 7.5 nm). The mean cluster size and dispersion from H_2 chemisorption were used to calculate turnover rates.

2.3. CO Hydrogenation Turnover Rates. CO hydrogenation rates were measured at 518−598 K in a U-shaped fritted quartz tube (8.1 mm i.d.). Temperatures were measured by a K-type thermocouple placed at the tube's external wall and kept constant using electronic controllers and a resistively heated furnace. CO conversions were kept below 5% to ensure differential conditions. Intraparticle and interparticle dilutions of Ru/SiO_2 with inert SiO_2 (Davisil grade 62; 75−109 μm; 340 m^2 g^{-1}; treated in flowing dry air at 1073 K for 3 h) confirmed the absence of heat or mass transfer corruptions, thus confirming that all measured rates reflect those of surface-catalyzed rates at the temperature and concentration of the contacting fluid phase (Supporting Information, SI; Section S1).[81] Intraparticle dilution was achieved by mixing Ru/SiO_2 and inert SiO_2 in 1:5−50 mass ratios; these mixtures were pelleted and sieved to retain 75−109 μm aggregates. The aggregates were then mixed physically with SiO_2 (75−109 μm) at 1:20−100 mass ratios. Measured CO turnover rates (5% wt. Ru/SiO_2, 7.5 nm clusters; 573 K; 2 kPa CO, 60 kPa H_2, 8 kPa H_2O, balance He) were unaffected by intraparticle (1:5 to 1:50) or interparticle (1:20 to 1:100) dilution (SI; Figure S1).

Reactant concentrations (H_2, Praxair, 99.999%; 90% CO/Ar; 1% CO/He; 31% CO/62% H_2/He; He, Praxair, 99.999%) were set using electronic mass flow controllers (Porter, type 201). H_2O (deionized) was introduced using a microsyringe pump (Cole Parmer, model 60061; Hamilton #1001 syringe) and vaporized into a flow of gaseous reactants. All transfer lines were kept above 400 K to prevent condensation. Passivated samples were treated in flowing 50% H_2/He (Praxair, 99.999%, 1.67 cm^3 g^{-1} s^{-1}) at 723 K (0.033 K s^{-1}) for 2 h before contact with reactants.

Reactant and product concentrations were measured by thermal conductivity (Agilent 3000A Micro GC) after separation by PoraPLOT Q and 5A sieve columns. CH_4, C_2H_4, C_2H_6, C_3H_6, C_3H_8, H_2O, and CO_2 were detected as products in the effluent stream. A calibrated gas mixture (Matheson, 1% CO, 1% CH_4, 1% CO_2, 1% C_2H_4, 1% C_2H_6, 1% C_3H_6, 1% C_3H_8, balance He) was used to obtain response factors. CO hydrogenation turnover rates (r_{CO}) are reported as the rate of conversion of CO molecules to all detected hydrocarbons; they do not include CO conversion to CO_2, which was formed at <5% selectivity. Rates are normalized per Ru surface atom as determined from H_2 chemisorption studies described in Section 2.2.

2.4. Infrared Spectra During CO Hydrogenation Catalysis. Infrared spectra (1100−4000 cm^{-1}; 1 cm^{-1} resolution; 64 scans) were collected using a Thermo Nicolet 8700 infrared spectrometer equipped with an Hg-Cd-Te (MCT) detector cooled by liquid N_2 during H_2-CO reactions. Passivated catalyst samples (1:10 intraparticle dilution, treated as described in Section 2.3) were used as self-supporting wafers (30−50 mg cm^{-2}) and held between CaF_2 windows within an in situ transmission infrared cell.[82] These wafers were treated in flowing 50% H_2/He (Praxair, 99.999%, 1.67 cm^3 g^{-1} s^{-1}) at 723 K (0.033 K s^{-1}) for 2 h (as in catalytic experiments, Section 2.3) before catalytic and infrared measurements. Infrared bands were deconvoluted using Gaussian−Lorentzian mixed functions.[83,84] The amount of CO* was determined from the integrated intensities of the CO* infrared bands during CO-H_2 reactions. CO hydrogenation turnover rates were measured by chromatographic analysis of the effluent from the infrared cell using the protocols described in Section 2.3.

2.5. Density Functional Theory Methods. Periodic plane-wave DFT methods implemented in the Vienna ab initio simulation package (VASP)[85−88] were used to calculate dispersion-corrected free energies of CO* and other relevant intermediates on full Ru_{586} clusters and their hemispherical Ru_{218} counterparts.[40]

Planewaves were constructed using projector augmented-wave (PAW) potentials with an energy cutoff of 400 eV.[89,90] The revised Perdew−Burke−Ernzerhof (RPBE) form of the generalized gradient approximation (GGA) was used to determine exchange and correlation energies for all calculations.[91−93] Dispersive interactions were incorporated into the energies of RPBE calculations using DFT-D3 with Becke and Johnson (BJ) damping;[94,95] dispersive interactions were calculated between adsorbed species, but not between the adsorbate species and the Ru_{218} surface atoms, because D3 methods are known to overpredict binding energies on metal surfaces.[40] Wave functions were converged to electronic energies $<10^{-6}$ eV; forces were determined using a fast Fourier transform (FFT) grid with a cutoff equal to twice the planewave cutoff. The Brillouin zone was sampled using the Γ-point.[96]

DOI: 10.1021/jacs.7b04606
J. Am. Chem. Soc. 2017, 139, 11789−11802

A Ru_{586} cuboctahedral particle (~2.5 nm in diameter) was optimized at three coverages (0.01, 1, and 1.04 ML) by relaxing all atoms to forces <0.05 eV/Å as described in more detail elsewhere.[40] These models were then simplified by removing the bottom six layers (in the (111) direction) to form Ru_{218} hemispherical particle models. The bottom two layers of these structures and the CO* bound to them were kept fixed during subsequent optimizations and transition-state searches to prevent structural rearrangement associated with the hemispherical nature of the model.

This Ru_{218} hemispherical model was then used to compute free energies for the H-assisted CO* activation pathway. All structural optimizations were performed with wave functions converged to $<10^{-6}$ eV and a FFT grid size twice the planewave cutoff and converged to a maximum force of <0.05 eV/Å on each unconstrained atom. Transition-state structures were found using nudged elastic band (NEB) methods[97,98] and then refined using dimer methods[99] for each elementary step. NEB methods used 16 images, and wave functions converged to 10^{-4} eV with a FFT grid 1.5 times the size of the plane-wave cutoff. Maximum forces on each atom were converged to <0.3 eV/Å for these NEB calculations. The dimer algorithm was then used with wave functions converged to $<10^{-6}$ eV and a FFT grid size twice the planewave cutoff and converged to a maximum force of <0.05 eV/Å on each atom (the same convergence criteria applied to optimizations).

Frequency calculations were carried out on all optimized states (including transition states) to determine zero-point vibrational energies (ZPVE), vibrational enthalpies (H_{vib}), and free energies (G_{vib}). The finite difference method was used with two displacements per unconstrained atom to calculate the Hessian matrix and vibrational frequencies of species involved in H-assisted CO* activation and the five spectating CO* nearest the active site (the center of the (111) terrace on the Ru_{218} particle, see Figure S2 in Section S2 of SI for more detail). These vibrational frequencies were used, together with VASP-derived electronic energies (E_0), to obtain enthalpies:

$$H = E_0 + E_d + \mathrm{ZPVE} + H_{vib} + H_{trans} + H_{rot} \quad (3)$$

and free energies:

$$G = E_0 + E_d + \mathrm{ZPVE} + G_{vib} + G_{trans} + G_{rot} \quad (4)$$

for all reactant, product, and transition-state structures, where E_d is the dispersive energy between all C, O, and H atoms estimated by DFT-D3(BJ) methods.[94,95] For gaseous molecules, translational and rotational enthalpies and free energies were computed from statistical mechanics. The equations used to determine ZPVE, H_{vib}, and G_{vib} from vibrational frequencies for all species and H_{trans}, H_{rot}, G_{trans}, and G_{rot} from statistical mechanics formalisms for gas-phase molecules are reported in the SI (Section S3; eqs S1–S13).

Dispersion-corrected potential (electronic) energies were also calculated using VASP (with spin-polarization) for a two-dimensional hexagonal CO lattice and for the kinetically relevant transition state ($HCO-H^{\ddagger}$)[38,48,49,54,60−65] within this lattice. A two-dimensional hexagonal lattice of CO was chosen as an arrangement that mimics the close-packed surfaces of fcc (111) and hcp (0001) metals. The C atoms in CO were kept fixed to preserve their close-packed structure and to prevent the migration of CO in the 'z'-direction. All O atoms were relaxed to forces <0.05 eV/Å. The $HCO-H^{\ddagger}$ transition-state structure was reported previously[40] from DFT calculations on Ru_{218} clusters at 1.04 ML CO*. The distance between CO molecules on the lattice was varied between 0.25 to 0.40 nm; this range includes the mean CO*−CO* distances on the (111) terraces of Ru_{586} clusters (~2.5 nm diameter) at 1.00 ML CO* (0.324 nm) and 1.04 ML CO* (0.308 nm), shown in Figure S3. Intermolecular CO−CO bond distances were varied in this lattice to probe the effects of CO* adlayer compression on the stability of $[*HCO-H^*]^{\ddagger}$ transition states and of the two CO* that must be removed from Ru surfaces to bind the transition state on surfaces densely covered with CO*. These effects of CO adlayer densification mimic the monotonic increase in CO* coverages that occurs as CO pressure increases even near saturation.

On nearly saturated surfaces, one CO* must desorb for H-assisted activation of a second vicinal CO via the $[*HCO-H^{*\ddagger}]$ transition state:[38−40]

$$2\,CO^* + H_2(g) \leftrightarrows [*HCO\text{–}H^*]^{\ddagger} + CO(g) \quad (5)$$

This stoichiometric reaction, based on the formalism of transition-state theory, reflects CO* activation rates that are limited by the free energy of formation for $[*HCO-H^{*\ddagger}]$ and CO(g) from two CO* and one H_2(g) at conditions of high CO* coverage as described by the asymptotic form of eq 1. The dispersion-corrected free energy was then calculated for eq 5 on a Ru_{218} hemispherical particle model at three coverages of spectator CO* (0, 1, and 1.04 ML). To assess the effects of adlayer densification on reaction rates, free energy barriers for eq 5 were calculated using a Ru_{218} hemispherical particle model and a two-dimensional hexagonal CO lattice. The inherent symmetry of the Ru_{218} cluster allows only discrete changes in CO* coverage without introducing disorder and the need to compute a very large number of possible configurations at a prohibitive computational cost, while the hexagonal CO lattice model used here allows continuous changes in adlayer density in response to changes in the chemical potential of CO in the gaseous phase.

3. RESULTS AND DISCUSSION

3.1. CO* Coverages from Infrared Spectra During CO-H_2 Reactions. The infrared spectra of chemisorbed species during CO hydrogenation were used to determine CO* coverages with concurrent measurements of turnover rates. Figure 2 shows representative spectra measured during reaction

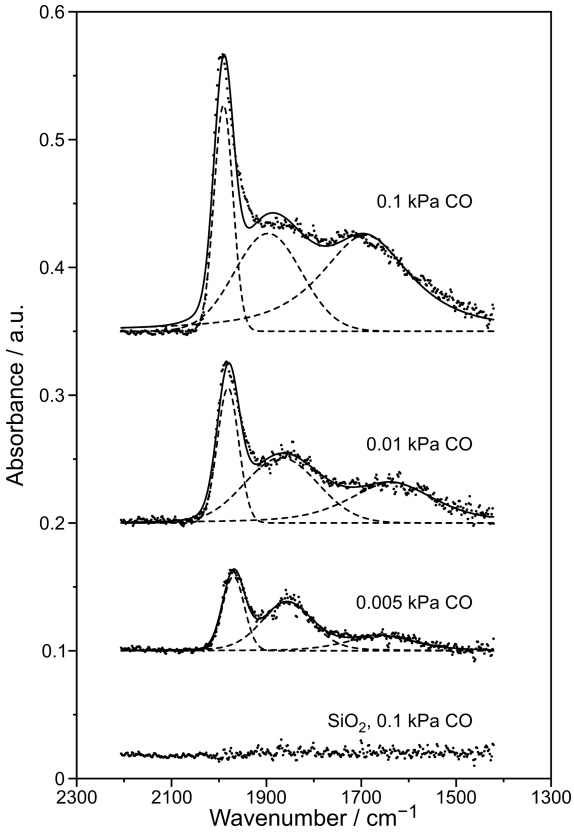

Figure 2. Infrared spectra (and the deconvoluted bands) during steady-state CO-H_2 reaction on SiO_2 and 5% wt. Ru/SiO_2 (7.5 nm Ru clusters, 1:10 intraparticle dilution; 573 K, 0.005−0.1 kPa CO, 0.1−2 kPa H_2, balance He; L-CO* for linear CO*, B-CO* for bridging CO*, M-CO* for CO*interacting with >2 Ru surface atoms).

DOI: 10.1021/jacs.7b04606
J. Am. Chem. Soc. 2017, 139, 11789−11802

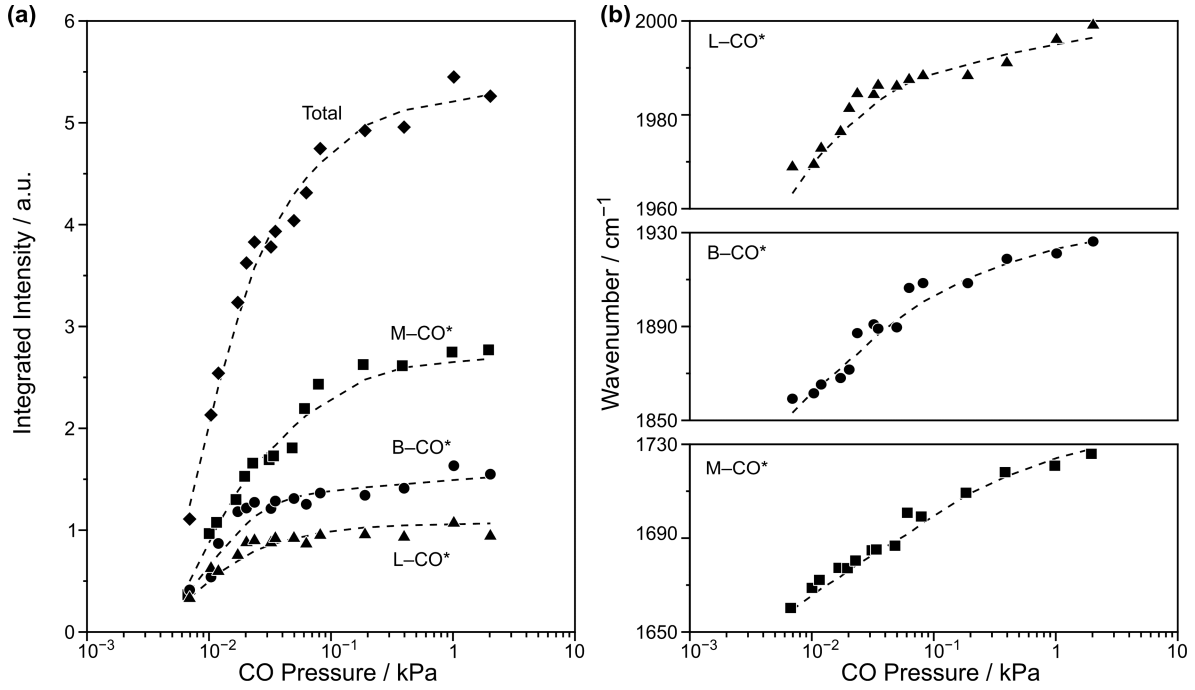

Figure 3. (a) Integrated intensities and (b) vibrational frequencies of C−O stretches for deconvoluted CO*-bands (L-CO*, B-CO*, and M-CO* as defined in Figure 2) as the function of CO pressure (0.1−2 kPa H_2, balance He) at 573 K on 5% wt. Ru/SiO_2 catalyst (7.5 nm clusters).

(0.005−0.1 kPa CO, 0.1−2 kPa H_2, balance He; 573 K) on 5% wt. Ru/SiO_2 catalyst (1:10 intraparticle dilution) treated in 50% H_2/He at 673 K before exposure to reactants; CO bands were not detected on the SiO_2 support (Figure 2). The three CO stretch bands (1500−2050 cm^{-1}, Figure 2) were assigned to linear atop CO* on a single Ru atom (L-CO*, 1950−2050 cm^{-1}), CO* bridging two vicinal Ru atoms (B-CO*, 1850−1950 cm^{-1}), and CO* interacting with three or more Ru atoms (M-CO*, 1500−1850 cm^{-1}).[100−103] DFT calculations of CO* stretch frequencies for a 1.04 ML CO* adlayer on the Ru_{218} hemispherical particle (Figure S2a) gave values of 2016 cm^{-1} for L-CO* species and 1878 cm^{-1} for B-CO* species, consistent with these assignments, although no M-CO* species were present in that simplified DFT model. All three CO bands shifted to higher frequencies and became more intense as the CO pressure increased from 0.005 to 0.1 kPa, indicative of coverages below saturation at these CO pressures and 573 K.

At such low coverages and pressures (<0.1 kPa CO), the integrated intensities of the three CO* bands and their respective C−O stretching frequencies increased with CO pressure (Figure 3). The shift in frequency at these low CO* coverages reflects a decrease in the extent of back-donation from the surface to the CO $2\pi^*$ molecular orbital[104,105] with increasing CO* coverage, which leads, in turn, to stronger C−O bonds. This increase in vibrational frequency was also predicted by DFT, as calculated L-CO* stretch frequencies increased by 8 cm^{-1} as CO* coverage increases from 1.00 to 1.04 ML for CO* bound to the low-index terrace of Ru_{218} hemispherical particle models. The three CO* bands (L, B, and M) evolved similarly in intensity with changes in CO pressure. All of these react at similar rates, as evident from their concurrent disappearance upon removal of CO from H_2-CO reactant flow, even at temperatures (418 K, SI, Section S4; Figure S4) well below those used for catalytic measurements (518−598 K). Thus, their combined intensities were used to determine CO* coverages.

Integrated CO* intensities increased about 4-fold as the CO pressure increased from 0.01 to 0.1 kPa (Figure 3a), in a manner consistent with the form of the Langmuir isotherm. Above 0.1 kPa CO, intensities continued to increase, but much more gradually, with increasing CO pressure, consistent with surfaces that approach CO* saturated coverages and with a monotonic lateral compression of the CO* adlayer. This type of compression indicates the binding of additional CO molecules, plausibly at low-coordination surface atoms present in small particles.[38,40,106] This adlayer compression is also evident from the continuous increase in C−O stretching frequencies (Figure 3b), indicating that CO* coverage continues to increase, thus weakening C−M bonds and strengthening dipole−dipole interactions among co-adsorbed CO*. Dipole−dipole coupling has been shown to decrease molar extinction coefficients for CO* bound to flat surfaces,[107−109] indicating that the change in slopes observed in Figure 3 could also be attributed to dipole−dipole coupling at high coverages. These dipole−dipole effects, however, are weaker on the curved surfaces of nanoparticles[110−114] and therefore may not have a major impact on the intensities reported herein, as evidenced by the strong agreement between measured and Langmuir-predicted intensities at CO* coverages beneath saturation (Figure 4).

Infrared spectra were measured on Ru/SiO_2 (5% wt.; 1:10 intraparticle dilution) during steady-state CO hydrogenation (518−598 K, 0.001−100 kPa CO, 1−60 kPa H_2, 0−32 kPa H_2O) to probe the effects of CO, H_2, and H_2O pressures on CO* coverages and the consequences of such coverages for reactivity. H_2 (1−60 kPa) and H_2O (0−32 kPa) pressures did not influence the intensity or the frequency of the CO infrared bands (SI, Figure S5), indicating that the coverages of adsorbed species derived from H_2 or H_2O (e.g., H*, O*, OH*, H_2O*) are much smaller than those of CO*. The invariance of the CO* adlayer with H_2 or H_2O pressure is consistent with previous studies on Ru,[35,39,38,115] Rh,[61] and Co[48,116,117] that

DOI: 10.1021/jacs.7b04606
J. Am. Chem. Soc. 2017, 139, 11789−11802

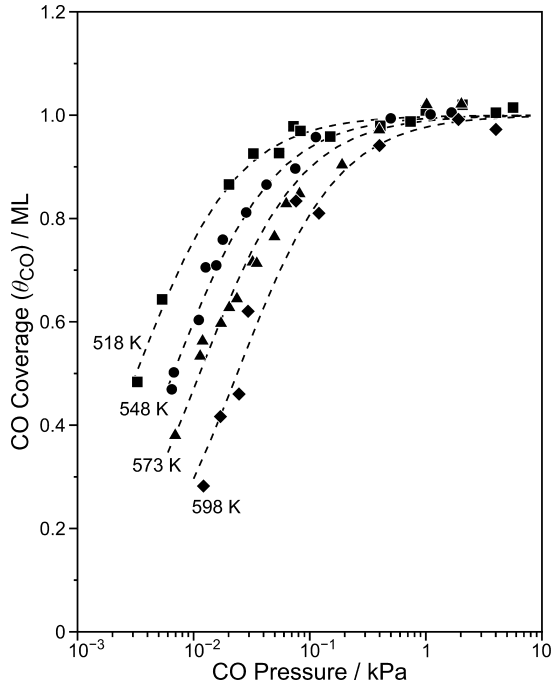

Figure 4. CO adsorption isotherms on 5% wt. Ru/SiO_2 (7.5 nm particles, 1:10 intraparticle dilution) at different temperatures (the dotted curves are the trends for Langmuir-type adsorption).

also showed the CO* conversion does not vary with time or conversion level, suggesting that C* and O* do not accumulate on surfaces during CO hydrogenation at these conditions.

Langmuir adsorption models lead to fractional CO* coverages (θ_{CO}) given by

$$\theta_{CO} = \frac{A}{A_{sat}} = \frac{K_{CO}P_{CO}}{1 + K_{CO}P_{CO}} \quad (6)$$

This equation adequately describes CO* coverages determined from the intensity of the infrared bands on Ru/SiO_2 (0.001−10 kPa CO; 518−598 K) at low CO pressures (<0.1 kPa), as shown by the dashed curves in Figure 4. In eq 6, A represents the combined integrated intensity of the three CO bands (2050−1500 cm^{-1}, Figure 2), while A_{sat} is the saturation absorbance obtained by regressing all integrated absorbances to the functional form of eq 6. K_{CO} is the coverage-independent CO adsorption constant that characterizes Langmuirian surface treatments. Langmuirian adsorption models (eq 6) do not account for co-adsorbate repulsion or dipole−dipole coupling of CO*, and becoming inaccurate as CO*−CO* distances shorten with increasing coverage. The fractional monolayer coverages (θ_{CO}), used here as convenient and customary proxies for CO*−CO* distances, were obtained by using a saturation coverage derived by extrapolation of the low-pressure CO band intensities to high CO pressures and CO* coverages using the Langmuirian form of the adsorption isotherm (eq 6).

The K_{CO} values were determined from CO* coverages at low CO pressures (<0.1 kPa, submonolayer CO* coverages) at four different temperatures (518, 548, 573, and 598 K). These data give a CO adsorption enthalpy of −63 ± 5 kJ mol^{-1} and an adsorption entropy of −73 ± 7 J mol^{-1} K^{-1} at these submonolayer coverages, which lead to K_{CO} values that can be treated as independent of coverage. Previously measured and calculated CO* adsorption enthalpies (−104 to −218 kJ mol^{-1} at CO* coverages ranging from 0−0.5 ML CO*)[38,118−121] are much more negative than those measured here (−63 kJ mol^{-1}), indicating that the CO* adsorption enthalpy measured here reflects high-coverage CO* adsorption data.

Langmuir surface models (eq 6) cannot account for CO* coverages above 1 ML coverages, and the measured K_{CO} values indicate that 0.99 ML coverages are achieved at 0.4−2 kPa CO at 518−598 K. These models are inconsistent with infrared bands that become more intense and shift to higher frequencies at higher pressures. Trends in the infrared spectra indicate that Ru surfaces do not fully "saturate"; instead CO* adlayers continue to densify as the CO pressure increases. This contrasts with theory[38,122,123] and ultrahigh vacuum and even high-pressure experiments[121,124−129] on single-crystal surfaces, which suggest that CO* coverages saturate at submonolayer levels (0.7−0.9 ML). Curved surfaces, as reported previously,[6,38,60]

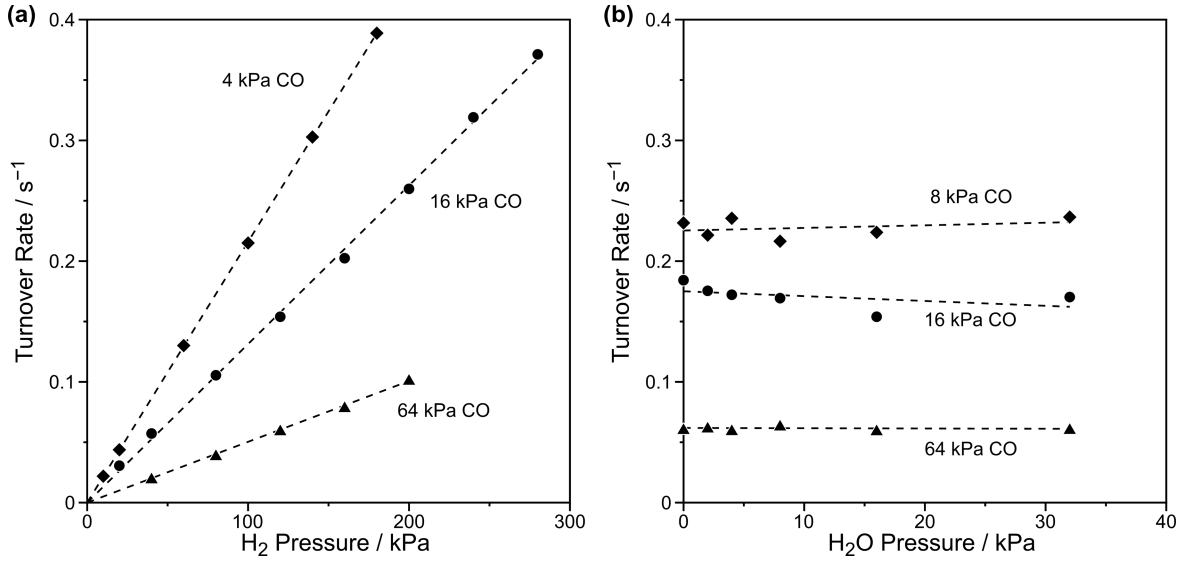

Figure 5. Effect of (a) H_2 (2−280 kPa H_2, 16 kPa H_2O) and (b) H_2O pressure (0−32 kPa H_2O, 120 kPa H_2) at different CO pressures (4−64 kPa) on CO hydrogenation turnover rates on 5% wt. Ru/SiO_2 (7.5 nm particle size, 1:10 intraparticle dilution) at 573 K.

DOI: 10.1021/jacs.7b04606
J. Am. Chem. Soc. 2017, 139, 11789−11802

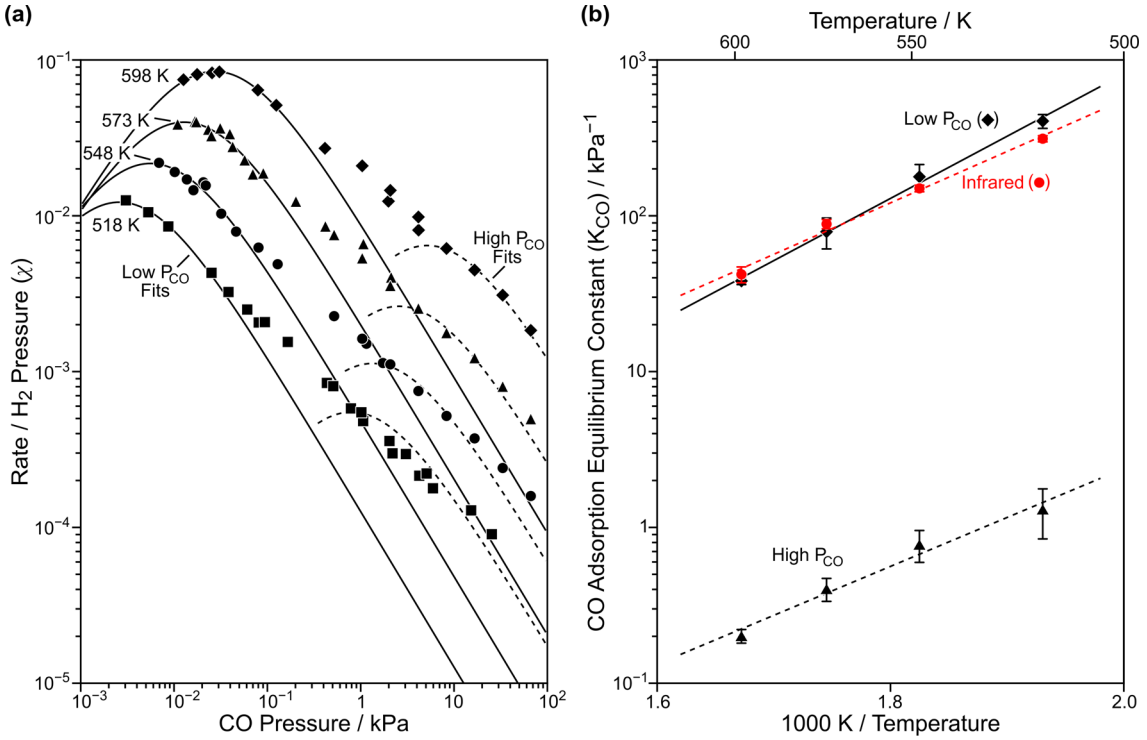

Figure 6. (a) Effect of CO pressure on CO-H_2 turnover rates (divided by H_2 pressure; χ, eq 7) on 5% wt. Ru/SiO_2 (7.5 nm) at 518−598 K. Solid lines show the rates predicted from eq 1 using K_{CO} values regressed from low-pressure rate data (which are nearly identical to those regressed from infrared data), and dashed lines show predicted rates using K_{CO} values regressed from high-pressure rate data. (b) Regressed CO adsorption constants (K_{CO}) from IR data (●), low-pressure rate data (10^{-3}−10^{-1} kPa CO, ◆), and high-pressure rate data (10−100 kPa CO, ▲).

weaken CO*−CO* repulsion through lateral relaxation, thus enabling higher CO* coverages to form. This type of adlayer densification is evident here at 0.1−1 kPa CO and 518−598 K and is even more significant at methanation conditions (1−100 kPa CO)[37,61] and much more so at the much higher CO pressures (~1 MPa CO) and lower temperatures (470−500 K) typical of FTS.[38,40] The strong CO*−CO* interactions that prevail are therefore relevant to the analysis of methanation and FTS turnover rates, which cannot be described with the coverage-independent K_{CO} values inferred from Langmuirian descriptions.

3.2. Effects of CO and H_2 Pressures on CO Hydrogenation Turnover Rates. CO hydrogenation turnover rates are shown in Figure 5 as a function of H_2 and H_2O pressures at 573 K. Turnover rates were proportional to H_2 pressure (20−280 kPa H_2, Figure 5a) at all CO pressures and temperatures, as also observed at the higher CO pressures typical of FTS reactions;[34,35,39,48,49,61] H_2O concentrations did not affect rates at these conditions (0−32 kPa H_2O; 573 K, Figure 5b). Similar kinetic effects of H_2 and H_2O were observed at all studied temperatures (518−598 K; SI, Figure S6). These trends allow us to describe the kinetic effects of CO pressure at all H_2 pressures by dividing rates by the H_2 pressure (χ):

$$\chi = \frac{r_{CO}}{P_{H_2}} \tag{7}$$

These values show that the kinetic order in CO evolves from positive to negative as CO pressure increases (0.01−100 kPa; Figure 6a) in a manner consistent with eq 1, as also reported over smaller CO pressure ranges and lower temperatures on Fe,[48,49] Co,[48,49] Ni,[43] Ru,[35,38,40,60,65] and Rh[61] catalysts.

At low CO pressures (0.001−0.1 kPa at 518−598 K), Langmuirian kinetic treatments (eq 1) accurately describe measured rates (solid curves in Figure 6a) using K_{CO} values that are nearly identical (Figure 6b) to those determined independently from CO* coverages derived from infrared bands (Figure 4, eq 6). The similar K_{CO} values obtained from kinetic and infrared data at low CO pressures show that Langmuirian models are appropriate, but only at the low CO* coverages (<0.8 ML) that prevail at these low-pressure conditions.

Very dense CO* adlayers, evident from infrared spectra at the higher CO pressures typical of methanation (1−100 kPa CO) or FTS (100−1000 kPa CO), would lead to rates described by a form of eq 1 in which CO* species become the most abundant surface intermediates ($K_{CO}P_{CO} \gg 1$):

$$r_{CO} = \frac{\alpha P_{H_2}}{K_{CO}^2 P_{CO}} = k_{app}\frac{P_{H_2}}{P_{CO}} \tag{8}$$

This asymptotic form of eq 1 cannot account, however, for the measured effects of CO pressure on FTS rates on Fe,[48,49] Co,[48,49] Ni,[43] Ru,[35,38,40,60,65] and Rh[61] catalysts. Inconsistencies in this model can be resolved only if k_{app} is allowed to increase monotonically as the CO pressure and the CO* adlayer density increase. A monotonic increase in k_{app} mimics the functional form of eq 1, but with an inappropriate chemical significance assigned to the value of k_{app}, as discussed in Section 3.3.

At higher CO pressures and CO* coverages, rates are much higher than expected from eq 1 using the K_{CO} values measured at lower pressures (Figure 6a); these deviations become stronger with increasing CO* coverages. Yet, rates can be adequately described by eq 1 at higher CO pressures (10−100 kPa CO) (dashed lines in Figure 6a), but with K_{CO} values that

DOI: 10.1021/jacs.7b04606
J. Am. Chem. Soc. 2017, 139, 11789−11802

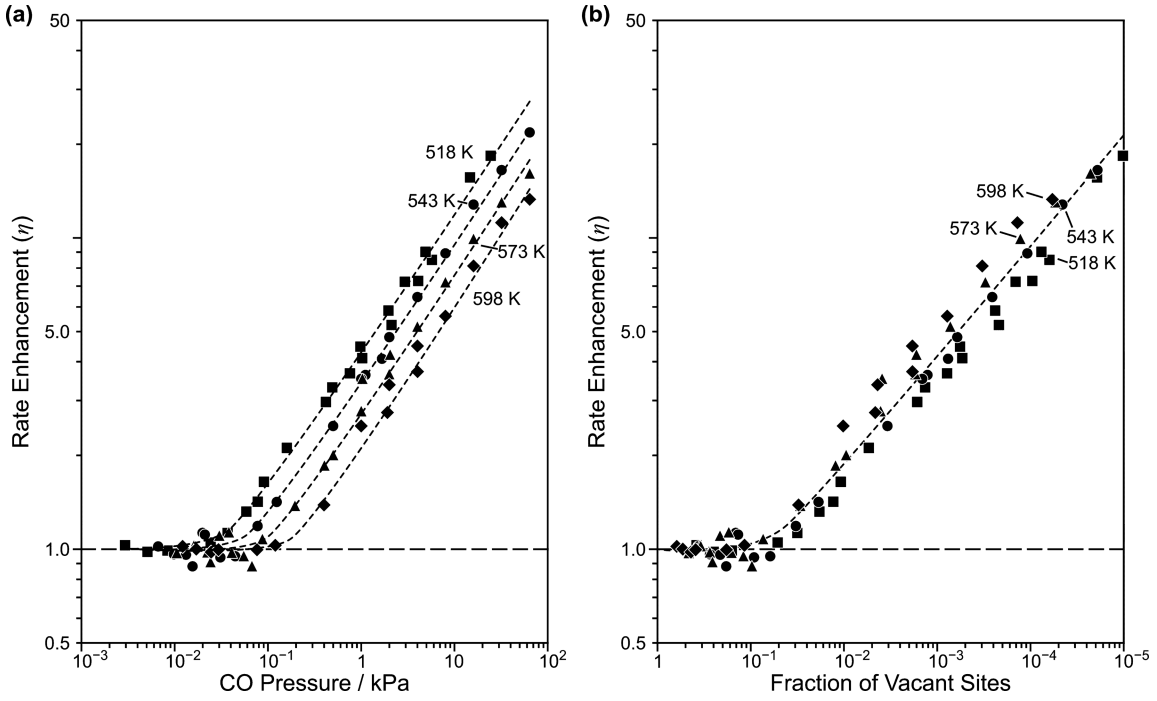

Figure 7. Ratios of measured to predicted CO hydrogenation rates (η, eq 9) as a function of (a) CO pressure and (b) CO* coverage (obtained from eq 6 with regressed K_{CO} value from IR data, Figure 4) on 5% wt. Ru/SiO_2 (7.5 nm particle size) at 518−598 K.

are about 200 times smaller than those derived from Langmuir treatments at lower CO pressures (Figure 6b). Rates at FTS conditions (518 K, 0.1−1.2 MPa CO)[38−40] on a similar catalyst (5% wt. Ru/SiO_2, 8 nm particles) can also be described adequately by eq 1, but with a K_{CO} value (0.005 kPa^{-1} at 518 K) that is 10^4 times smaller than those obtained from Langmuir treatments at lower CO pressures (Figure 6b). The K_{CO} equilibrium constants regressed from eq 1 are clearly not "constant" with CO pressure or CO* coverage at the conditions used to obtain the rate data reported to obey eq 1 in previous studies.[38,48,49,61] Eq 1, derived from Langmuirian treatments of surfaces, cannot capture the strong effects of co-adsorbate interactions that prevail as CO* adlayers densify with increasing CO pressure.

The enhancements in rates over those predicted by eq 1 with K_{CO} values at low coverages (η):

$$\eta = \frac{r_{CO,meas.}}{r_{CO,pred.}} \tag{9}$$

increased from a value of unity at submonolayer CO* coverages to values of 5−10 at 10 kPa CO and 518−598 K (Figure 7). Deviations from unity become evident at lower CO pressures as the reaction temperature decreases (Figure 7a), because the exothermic nature of CO chemisorption leads to equilibrium coverages that increase as the temperature decreases. Figure 7b shows that η values depend similarly on CO* coverage at all temperatures (518−598 K). These rate enhancements are described next in terms of the relative stability of CO* and of the kinetically relevant transition state as CO adlayers densify to probe the significant consequences for the K_{CO} and α parameters in eqs 1 and 8.

3.3. Mechanistic Interpretations of the Effects of CO* Coverage on CO Hydrogenation Turnover Rates on Ru Clusters. The effects of adlayer density on turnover rates were examined using transition-state theory applied to surfaces

Scheme 1. Elementary Steps for H-Assisted CO Activation Routes in CO Hydrogenation Reactions[a]

$$CO(g) + * \rightleftharpoons CO* \qquad K_{CO} \qquad (1)$$

$$H_2(g) + 2\,* \rightleftharpoons 2\,H* \qquad K_{H_2} \qquad (2)$$

$$CO* + H* \rightleftharpoons HCO* + * \qquad K_{CO^*\text{-}H^*} \qquad (3)$$

$$HCO* + H* \longrightarrow *HCOH* \qquad k_{HCO^*\text{-}H^*} \qquad (4)$$

$$*HCOH* \longrightarrow CH* + OH* \qquad k_{*,HCOH^*} \qquad (5)$$

$$CH* + 3\,H* \rightarrow\rightarrow CH_4* + 3\,* \qquad (6)$$

[a]An * denotes unoccupied surface sites; double arrow with a circle indicates a quasi-equilibrated step; K and k are equilibrium and rate parameters, respectively, for each elementary step.

rendered thermodynamically nonideal by strong co-adsorbate interactions that prevail at CO* coverages near saturation. The elementary steps involved in H-assisted CO* activation shown in Scheme 1 lead to rates described by the functional form of eq 1 (derived in Section S7; SI; eqs S14−S23). These steps are consistent with theoretical treatments of CO hydrogenation elementary steps on close-packed Ru(111),[38] Fe(110),[48,49] and Co(0001)[48,49] surfaces.

CO hydrogenation rates per exposed Ru atom depend on the fraction of Ru atoms that contain a transition state for the kinetically relevant *HCOH* formation step (Step 4, *HCO−H*‡). The quasi-equilibrated nature of Steps 1−3 allows them to be lumped as one nonelementary step, in which one H_2(g) and one CO(g) form the transition state that mediates Step 4:

$$CO(g) + H_2(g) + 2* \rightleftharpoons *HCO\text{–}H*^{\ddagger} \tag{10}$$

CO conversion turnover rates are then given by[130]

DOI: 10.1021/jacs.7b04606
J. Am. Chem. Soc. 2017, 139, 11789−11802

$$r_{CO} = \frac{k_B T}{h} K^{\ddagger} \frac{\gamma_*^2}{\gamma^{\ddagger}} P_{H_2} P_{CO} \theta_*^2 \quad (11)$$

where $K^{\ddagger}$ is the equilibrium constant for the stoichiometric reaction represented by eq 10 at coverages that avoid repulsive co-adsorbate interactions for either *HCO−H*‡ or the sites of the catalyst surface (*). The $\gamma_{\ddagger}$ and γ_* terms represent the activity coefficients that account for nonidealities for *HCO−H* and (*) in the dense adlayers present on the Ru surface, and θ_* is the fractional coverage of vacant sites at Ru surfaces. The molecular adsorption of CO (Step 1; Scheme 1) is quasi-equilibrated:

$$K_{CO} = \frac{\gamma_{CO*}}{\gamma_*} \frac{[CO^*]}{[*]P_{CO}} \quad (12)$$

and the substitution of this thermodynamic relation into eq 11 gives

$$r_{CO} = \frac{k_B T}{h} \frac{K^{\ddagger}}{K_{CO}^2} \frac{\gamma_{CO^*}^2}{\gamma_{\ddagger}} \frac{P_{H_2}}{P_{CO}} \theta_{CO}^2 \quad (13)$$

At near saturation coverages (P_{CO} > 1 kPa; $\theta_{CO} \approx 1$), this rate equation becomes

$$r_{CO} = \frac{k_B T}{h} \frac{K^{\ddagger}}{K_{CO}^2} \frac{\gamma_{CO^*}^2}{\gamma_{\ddagger}} \frac{P_{H_2}}{P_{CO}} \quad (14)$$

where $K^{\ddagger}$ and K_{CO} are the equilibrium constants for the reaction in eq 10 and for Step 1 in Scheme 1, respectively. Their magnitudes do not depend on CO* coverage because they correspond to the thermodynamically ideal context of these treatments. The activity coefficients (γ_{CO*} and $\gamma_{\ddagger}$), in turn, depend on CO* coverages, but not on *HCO−H*‡ coverages, because of the dilute nature of transition states within the dense CO* adlayer.

Eq 14 and the high-coverage form of eq 1 (eq 8) depend similarly on H_2 and CO pressures, but, in the case of eq 14, with an apparent rate constant (k_{app}) given by

$$k_{app} = \frac{k_B T}{h} \frac{K^{\ddagger}}{K_{CO}^2} \frac{\gamma_{CO^*}^2}{\gamma_{\ddagger}} \quad (15)$$

This apparent rate constant depends on CO* coverage through the $\frac{\gamma_{CO^*}^2}{\gamma_{\ddagger}}$ term, which reflects the co-adsorbate interactions within the CO* adlayer as it densifies with increasing CO pressure. The enhancement factor (η, eq 9) then becomes

$$\eta = \frac{k_{app}}{k_{ideal}} = \frac{\gamma_{CO^*}^2}{\gamma_{\ddagger}} \quad (16)$$

The effect of CO pressure on η is given by

$$\left(\frac{\partial \ln(\eta)}{\partial P_{CO}}\right)_T = \left(\frac{\partial \ln(\eta)}{\partial \tau}\right)_T \left(\frac{\partial \tau}{\partial P_{CO}}\right)_T \quad (17)$$

where τ represents the surface pressure (force per distance) exerted by adsorbed CO* on co-adsorbed species.[131] The surface pressure is analogous to the three-dimensional pressure used to account for similar forces on reaction volumes for homogeneous systems.[27−33,131] Such surface pressures must increase monotonically with increasing CO* coverages and thus with CO pressure ($\left(\frac{\partial \tau}{\partial P_{CO}}\right)_T > 0$). The change in enhancement factor (η) with CO pressure can be expressed in terms of an activation area (ΔA_{act}) at low coverages (ΔA_{act}^0) and how it changes with increasing surface pressure ($\Delta\Delta A_{act}$):

$$\left(\frac{\partial \ln(\eta)}{\partial P_{CO}}\right)_T = -\left[\frac{\Delta A_{act}^0 + \Delta\Delta A_{act}}{RT}\right] \times \left(\frac{\partial \tau}{\partial P_{CO}}\right)_T \quad (18)$$

as CO pressure increases (as derived in Section S8; SI; eqs S24−S35). The term in square brackets in eq 18 represents the activation area at a specific surface pressure, and its sign determines whether η increases or decreases as adlayers densify, in the same manner as activation volumes determine how hydrostatic pressure influences rates for liquid-phase reactions.[27−33,131]

A DFT-derived activation area can be estimated from CO* and [*HCO−H*]‡ structures optimized on close-packed terraces of Ru_{218} clusters at low coverages (0 spectating CO*, 0.02 ML) and high coverages (106 and 110 spectating CO* per 106 Ru surface atoms, 1.00 and 1.04 ML). Surface areas of each adsorbed species are taken as the area of the Ru surface occluded by their atoms, with atomic sizes determined by their van der Waals radii[132] (Table 1). At low coverages (no spectator CO* species), the CO* and *HCO−H*‡ areas are 0.0796 nm^2 and 0.1237 nm^2, respectively, thus giving an activation area of −0.0356 nm^2. At higher spectator CO* coverages (1.04 ML; Figure 8), the CO* and *HCO−H*‡ species both become slightly smaller, but both species contract similar amounts. As a result, the activation areas are essentially identical on bare surfaces and on those with 1.04 ML CO* (−0.0356 vs −0.0357 nm^2). Thus, the term in brackets in eq 18

Table 1. Activation Areas at Low (0.02 ML) and High (1 and 1.04 ML) CO* Coverage

spectating θ_{CO} (ML)	A_{CO^*} (nm^2)	$A_{\ddagger}$ (nm^2)	ΔA_{act}[a] (nm^2)
0.00	0.0796	0.1237	−0.0356
1.00	0.0798	0.1210	−0.0386
1.04	0.0787	0.1217	−0.0357
ΔA[b] (0.00 → 1.04 ML)	−0.0009	−0.0020	+0.0013

[a]Activation area (SI; eq S33) associated with forming the *HCO−H*‡ from a pair of co-adsorbed CO*. [b]Change in area (ΔA) or activation area ($\Delta\Delta A_{act}$) observed as CO* coverage shifts from 0.02 to 1.04 ML.

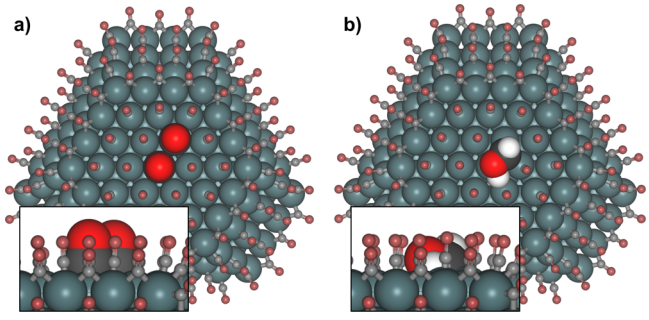

Figure 8. (a) Two chemisorbed CO species (CO*) and (b) the kinetically relevant [*HCOH*]‡ transition state on CO*-covered (1.04 ML) surfaces of a Ru nanoparticle shown using their van der Waals radii.

DOI: 10.1021/jacs.7b04606
J. Am. Chem. Soc. 2017, 139, 11789−11802

remains negative at all CO* coverages, and η values increase monotonically as CO* coverages (and CO pressures) increase.

Eqs 17 and 18 are analogous to those derived using similar formalisms to account for the effects of (hydrostatic) pressure in homogeneous reactions occurring in the liquid or gas phase and mediated by intermediates present in their thermodynamically nonideal states.[27−33,131] These formalisms are translated here into concepts of adlayer compression and two-dimensional lateral pressure to describe chemical reactions occurring on densely covered surfaces.[131]

Next, we estimate the magnitudes of the enhancement factors (η) and the k_{app} values (eq 15) caused by CO* adlayer densification as consequence of the negative activation area for these CO hydrogenation reactions. Such estimates are obtained using DFT methods to calculate effective free energy barriers using a hemispherical Ru_{218} cluster at three distinct coverages of spectator CO* (0, 1.00, and 1.04 ML) and a two-dimensional hexagonal CO lattice to probe the effects of a monotonic increase in CO* surface density.

3.4. DFT Calculations of Activation Energies As the Density of CO* Adlayer Increases. The lumped rate constant (k_{ideal}, eq 16) for the thermodynamically ideal case is defined using Langmuir treatments as

$$k_{ideal} = \frac{k_B T}{h}\frac{K^{\ddagger}}{K_{CO}^2} = \exp\left(-\frac{\Delta G^{0\ddagger}}{RT}\right) \quad (19)$$

where $\Delta G^{0\ddagger}$ is defined as the free energy to form the [HCO−H‡] structure from two co-adsorbed CO* and H_2 (eq 5) using free energies for the respective species in their thermodynamically ideal state (adsorbed species without co-adsorbate interactions and ideal gases). Similarly, nonideal systems are described by a rate constant (k_{app}) determined by $\Delta G^{\ddagger}$ values that account for co-adsorbate interactions and therefore vary with CO* coverage. The rate enhancement factor (η) is given by the ratio of activity coefficients (eq 16), which is related to the activation free energies for the ideal ($\Delta G^{0\ddagger}$) and the nonideal ($\Delta G^{\ddagger}$) surfaces:

$$\frac{\gamma_{CO^*}^2}{\gamma_{\ddagger}} = \exp\left(\frac{-(\Delta G^{\ddagger} - \Delta G^{0\ddagger})}{RT}\right) \quad (20)$$

$\Delta G^{\ddagger}$ and $\Delta G^{0\ddagger}$ differ because co-adsorbate interactions affect the free energies of CO* (ΔG_{CO^*}) and the transition state ($\Delta G_{*HCO-H^{*\ddagger}}$):

$$\Delta G_{CO^*} = G[CO^*] - G^0[CO^*] \quad (21)$$

$$\Delta G_{*HCO-H^{*\ddagger}} = G[{}^*HCO - H^{*\ddagger}] - G^0[{}^*HCO - H^{*\ddagger}] \quad (22)$$

to different extents. Eq 20 can then be rewritten as

$$\frac{\gamma_{CO^*}^2}{\gamma_{\ddagger}} = \exp\left(\frac{2\Delta G_{CO*} - \Delta G_{*HCO-H^{*\ddagger}}}{RT}\right) \quad (23)$$

in terms of the difference in co-adsorbate interactions between CO* and [*HCO−H*]‡.

The free energies for the H-assisted CO* activation mechanism (Steps 1−5 in Scheme 1) were calculated at three coverages. The "ideal" $\Delta G^{\ddagger}$ value ($\Delta G^{0\ddagger}$) corresponds to a surface without co-adsorbate interactions; thus, the species involved were treated as isolated entities on close-packed terraces of Ru_{218} particles without spectator CO* species. The CO* desorption free energy is 79 kJ mol^{-1} on such bare surfaces, while the activation free energy ($\Delta G^{0\ddagger}$) is 280 kJ mol^{-1} (Figure 9). The free energy to desorb CO* decreases

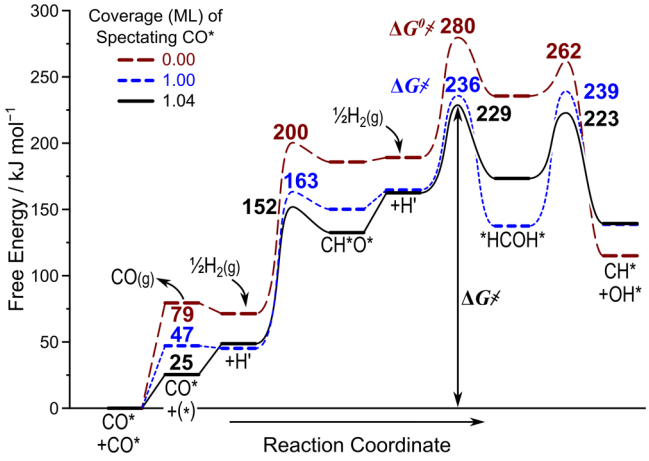

Figure 9. Free energy reaction coordinate diagram for H-assisted CO activation (Scheme 1) on a Ru_{218} half-particle catalyst model at various CO* coverages. Free energies of activation, $\Delta G^{0\ddagger}$ and $\Delta G^{\ddagger}$, shown here reflect the free energies for forming the [*HCO−H*]‡ transition state from two CO* (eq 5) with ($\Delta G^{\ddagger}$) and without ($\Delta G^{0\ddagger}$) co-adsorbed CO*.

from 79 kJ mol^{-1} on bare surfaces to 25 kJ mol^{-1} at 1.04 ML (Figure 9) because of repulsive CO*−CO* interactions. High CO* coverages also destabilize the *HCO−H*‡ transition state, but presumably to a lesser extent than the pair of CO* which it replaces, because of the negative activation area for this reaction (Table 1). Indeed, $\Delta G^{\ddagger}$ values decreased from 280 kJ mol^{-1} on bare surfaces to 229 kJ mol^{-1} at 1.04 ML (Figure 9). These calculations are consistent with the rate enhancements (η, eq 16, Figure 7) and lower activation free energies ($\Delta G^{\ddagger}$) measured as CO* adlayers densify with increasing CO pressure, a consequence of the negative activation area for H*-assisted CO* activation. This DFT model, specifically the CO* adlayer, is a simplified approximation of the real surface, which has CO* bound to three distinct sites at all coverages (Figure 2). Nevertheless, the predicted decrease in $\Delta G^{\ddagger}$ and the corresponding agreement with kinetic data (Figure 7) indicates that the multisite nature of the real CO* adlayer does not significantly alter the effects of CO* coverage on the reaction kinetics.

The effects of adlayer compression on reactivity reflect the effects of co-adsorbate repulsion within the adlayer, which are sensed by CO* and [*HCO−H*]‡ to different extents. Ru_{218} clusters can be examined only at a few discrete coverages, because intermediate coverages would require calculations of very large systems (>2800 electrons) for many configurations of adsorbed species, thus precluding the analysis of monotonic changes in CO* coverages. A continuous assessment of CO* coverage effects is carried out here using a two-dimensional hexagonal CO lattice (lg) model (depicted in Figure 10b) to calculate the energies of CO* and [*HCO−H*]‡ as the CO lattice is laterally compressed (mimicking the decrease in CO*−CO* distances that occurs with increasing CO* coverage/adlayer density). The energy barrier ($\Delta E^{\ddagger lg}$) to form HCO−H‡(lg) from 2 CO(lg) and stoichiometric amounts of gas-phase H_2 and CO (eq 10) is given by

DOI: 10.1021/jacs.7b04606
J. Am. Chem. Soc. 2017, 139, 11789−11802

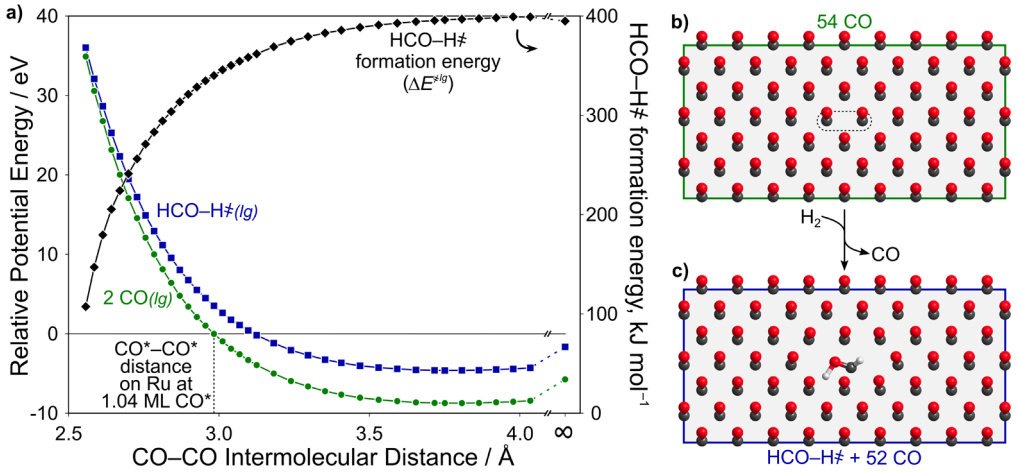

Figure 10. (a) Change in potential energies (relative to a hexagonal CO lattice with an intermolecular distance of 2.97 Å) for 2 CO in a hexagonal lattice of 54 total CO, (shown in part b) and the HCO–H‡ transition-state structure in a CO lattice (shown in part c) as a function of intermolecular CO distances. The HCO–H‡ transition-state formation energy ($\Delta E^{lg‡}$) is shown in the right-hand axis of part a.

$$\Delta E^{‡lg} = E[\mathrm{HCO-H^{‡}(lg)}] + E[\mathrm{CO(g)}] - 2E[\mathrm{CO(lg)}] - E[\mathrm{H_2(g)}] \quad (24)$$

The CO lattice model cannot describe M–CO* vibrations, because no metal atoms are present, thus preventing sensible entropy estimates and restricting our analysis to potential energies for HCO–H‡ and CO within the lattice. At large CO–CO distances (>0.55 nm), the $\Delta E^{‡lg}$ (eq 24) is 394 kJ mol^{-1}, a value much larger than on Ru (111) facets of clusters (280 kJ mol^{-1} at 0.02 ML (Figure 9)), because this lattice model does not include the stabilization by a binding surface. The CO(lg) and HCO–H‡(lg) energies increase as CO–CO distances become shorter (Figure 10a), because both species are destabilized by repulsive interaction with vicinal CO(lg) molecules. These effects are stronger for CO(lg) than for HCO–H‡(lg); this leads to a decrease in activation barrier ($\Delta E^{‡lg}$) as the CO* adlayer densifies (Figure 10a), as also shown on more realistic surfaces, for which free energy barriers ($\Delta G^{‡}$) decreased as the CO* coverage increased from bare surfaces to 1.04 ML CO* (Figure 9).

Calculations on CO*-covered Ru_{586} clusters are used to relate CO–CO distances in the CO lattice model to specific surface coverages. The mean CO*–CO* distance is 0.324 nm on the close-packed terraces of Ru_{586} nanoparticles at 1 ML CO* (Figure S3); these distances represent the average of the C–C (0.314 nm) and O–O (0.335 nm) distances among CO* (the larger O–O distances reflect surface curvature). At this CO–CO distance (0.324 nm), the $\Delta E^{‡lg}$ value is 374 kJ mol^{-1}, which is 20 kJ mol^{-1} lower than at noninteracting CO* distances in the lattice model. A very small increase in CO* coverages (from 1.0 to 1.04 ML by adding 12 CO* to the edges and corners of Ru_{586} clusters) decreased the mean CO*–CO* distance from 0.324 to 0.308 nm (Figure S3) and $\Delta E^{‡lg}$ values from 374 to 354 kJ mol^{-1} in the lattice model, an additional decrease from the 394 kJ mol^{-1} obtained for noninteracting CO* in the lattice model.

The stronger repulsive effects felt by CO* than by *HCO–H*‡ lead to the observed rate enhancements as the CO* adlayer is compressed with increasing CO pressure (Figure 7), and this is captured by the CO lattice model, despite the lack of metal catalyst present in that model, indicating that purely through-space repulsions can explain the promotional effects of CO* coverage on CO* activation rates. Table 2 shows $\Delta G^{‡}$ (calculated on Ru_{218}) and $\Delta E^{‡lg}$ values calculated at three

Table 2. Activation Free Energies at Various CO* Coverages from the Ru_{218} Model ($\Delta G^{‡}$) and from the CO Lattice ($\Delta E^{‡lg}$)

spectating θ_{CO} (ML)	$\Delta G^{‡}$ (kJ mol^{-1})	CO–CO (pm)	$\Delta E^{‡lg}$ (kJ mol^{-1})
0.00	280	>570	394
1.00	236	324	374
1.04	229	308	354
spectating θ_{CO} (ML)	$\Delta\Delta G^{‡a}$	CO–CO (pm)	$\Delta\Delta E^{‡lg a}$
0.00 → 1.00	−44	570 → 324	−20
1.00 → 1.04	−7	324 → 308	−20

[a]Changes in $\Delta G^{‡}$ or $\Delta E^{lg‡}$ as spectating CO* coverage (or the equivalent CO–CO distance in the CO lattice) changes from 0.00 to 1.00 ML and from 1.00 to 1.04 ML.

different CO* coverages on the Ru_{218} model and their corresponding CO–CO intermolecular distances in the CO lattice model. The CO lattice model cannot quantitatively predict the decreases in $\Delta G^{‡}$ (calculated on Ru_{218}) as CO* coverage increases (Table 2) because of the lack of through-surface co-adsorbate interactions and the lack of curvature, which alters CO–CO interactions. These through-surface and curvature effects are seen most dramatically for the shift from 0 to 1 ML coverage of spectating CO*, in which the electronic nature of the Ru particle is significantly altered by the adsorption of 106 CO* species, resulting in a large difference (24 kJ mol^{-1}) between the $\Delta\Delta G^{‡}$ values on the Ru_{218} and CO lattice models (Table 2). This CO lattice model does, however, capture through-space co-adsorbate interactions and qualitatively describes the decrease in activation free energies ($\Delta G^{‡}$) with increasing coverage and the increase in measured enhancement factors (η, eq 16) with increasing CO pressure. Lattice models, such as this one, can therefore be used to determine qualitative effects of co-adsorbate coverage (whether barriers increase or decrease) for other reactions, such as CO oxidation on Pd, where inconsistent kinetic data[133,134] have complicated mechanistic interpretations, leading to unsupported proposals that "reverse spillover" of CO* suppresses oxidation rates.

DOI: 10.1021/jacs.7b04606
J. Am. Chem. Soc. 2017, 139, 11789–11802

4. CONCLUSIONS

Kinetic and spectroscopic assessments of CO hydrogenation on supported Ru clusters (5% Ru/SiO_2, 7.5 nm Ru) show significant effects of CO* coverages on the rate of CO hydrogenation. CO-H_2 turnover rates are proportional to H_2 pressure and unaffected by H_2O pressure at all conditions studied here, while CO has a small effect on rates at low CO pressures and inhibits rates at high CO pressures, consistent with a rate equation (eq 1) that has been shown to predict kinetic data for CO-H_2 reactions on Co and Ru catalysts at the low CO pressures of this study (<100 kPa) and the high CO pressures associated with FTS (>100 kPa).

At low CO* coverages (<0.1 kPa CO), co-adsorbate interactions are negligible, allowing Langmuirian descriptions of surfaces to accurately predict CO isotherms and CO-H_2 turnover rates with consistent CO adsorption equilibrium constants (K_{CO}) obtained from these independent data sets. Ru surfaces become nearly saturated by CO* near 0.1 kPa CO. Langmuir adsorption models predict coverages of 1 ML at those pressures, but infrared CO* peak intensities and frequencies continue to increase slightly with increasing CO pressure, indicating that surfaces continue to densify at higher CO pressures. The high CO* coverages present at >0.1 kPa CO result in co-adsorbate interactions which prevent accurate descriptions by Langmuirian descriptions of surfaces. Here, we derive rate equations in these nonideal regimes by using transition-state theory and including activity coefficients which account for co-adsorbate interactions. Rates of CO* activation depend on the free energy difference between the kinetically relevant transition state ($[*HCO-H*]^{\ddagger}$) and a pair of co-adsorbed CO*. The transition state occupies less surface area than the pair of CO* which it replaces, resulting in a negative activation area, which increases the apparent rate constant for CO-H_2 reactions as CO* coverage increases with increasing CO pressure. These effects are observed here by an examination of CO-H_2 reactions at conditions which include submonolayer CO* coverages and saturated CO* surfaces within a single study by varying CO pressure over 4 orders of magnitude (0.01 to 100 kPa). This study resolves inconsistencies between ultrahigh-vacuum and high-pressure studies and DFT modeling of CO-H_2 reactions by describing how CO* coverage varies between these regimes and its concomitant effects on rates. Parallel studies have resulted in similar results for CO-H_2 reactions on smaller Ru particles (Ru/SiO_2, 1.8 and 3.5 nm)[65] and Co particles (Co/SiO_2).[46] Similar CO* coverage effects were also observed previously during CO* oxidation[1−8] and oxygenate decarbonylation[11,19,70] studies on metal surfaces at high adsorbate coverages, indicating the findings herein address a larger problem within catalysis.

ASSOCIATED CONTENT

Supporting Information

The Supporting Information is available free of charge on the ACS Publications website at DOI: 10.1021/jacs.7b04606.

Elimination of heat- and mass-transfer effects, details of DFT calculations models, transient FTIR details and results, effects of H_2 and H_2O on CO-H_2 rates and CO* coverages, detailed derivation of CO hydrogenation rate equation and the effects of activation areas on enhancement factors (PDF)

AUTHOR INFORMATION

Corresponding Authors

*hibbitts@ufl.edu

*iglesia@berkeley.edu

ORCID

Enrique Iglesia: 0000-0003-4109-1001

Notes

The authors declare no competing financial interest.

ACKNOWLEDGMENTS

The financial support of BP p.l.c. as part of the XC2 program and of the U.S. Department of Energy, Office of Science, Office of Basic Energy Sciences (under contract DE-AC05-76RL0-1830) is gratefully acknowledged. J.L. acknowledges a visiting research fellowship from China Scholarship Council (No. 201306450021). J.L. also thanks Prof. Fabio Toniolo (Federal University of Rio de Janeiro, Brazil) for his guidance with the in situ FTIR experiments, Prof. Prashant Deshlahra (Tufts University, Boston) for his advice on the quantification of infrared spectroscopy, and Dr. Xuebing Li (Chinese Academy of Sciences) and Prof. Honghong Shan (China University of Petroleum). Manuscript reviews and proofreading from Sarika Goel, Edwin Yik, Allie Landry, Iker Agirrezabal-Telleria, and Stephanie Kwon (University of California, Berkeley); Pavlo Kravchenko, Abdul Almithn, and Alex Hoffman (University of Florida) and Prof. Thomas Schwartz (University of Maine) are gratefully acknowledged.

REFERENCES

(1) Piccinin, S.; Stamatakis, M. *Top. Catal.* **2017**, *60*, 141−151.

(2) Gao, F.; McClure, S. M.; Cai, Y.; Gath, K. K.; Wang, Y.; Chen, M. S.; Guo, Q. L.; Goodman, D. W. *Surf. Sci.* **2009**, *603*, 65−70.

(3) García-Diéguez, M.; Iglesia, E. *J. Catal.* **2013**, *301*, 198−209.

(4) Dobrin, S. *Phys. Chem. Chem. Phys.* **2012**, *14*, 12122−12129.

(5) Boudart, M.; Djéga-Mariadassou, G. *The Kinetics of Heterogeneous Catalytic Reactions*; Princeton University Press: Princeton, NJ, 1984.

(6) Allian, A. D.; Takanabe, K.; Fujdala, K. L.; Hao, X.; Truex, T. J.; Cai, J.; Buda, C.; Neurock, M.; Iglesia, E. *J. Am. Chem. Soc.* **2011**, *133*, 4498−4517.

(7) Stamatakis, M.; Piccinin, S. *ACS Catal.* **2016**, *6*, 2105−2111.

(8) Araya, P.; Porod, W.; Sant, R.; Wolf, E. E. *Surf. Sci.* **1989**, *208*, L80−L90.

(9) Chin, Y.-H.; Buda, C.; Neurock, M.; Iglesia, E. *J. Am. Chem. Soc.* **2011**, *133*, 15958−15978.

(10) Getman, R. B.; Schneider, W. F.; Smeltz, A. D.; Delgass, W. N.; Ribeiro, F. H. *Phys. Rev. Lett.* **2009**, *102*, 076101.

(11) Gürbüz, E. I.; Hibbitts, D. D.; Iglesia, E. *J. Am. Chem. Soc.* **2015**, *137*, 11984−11995.

(12) Zhuo, M.; Borgna, A.; Saeys, M. *J. Catal.* **2013**, *297*, 217−226.

(13) Lausche, A. C.; Medford, A. J.; Khan, T. S.; Xu, Y.; Bligaard, T.; Abild-Pedersen, F.; Nørskov, J. K.; Studt, F. *J. Catal.* **2013**, *307*, 275−282.

(14) Dumesic, J. A.; Rudd, D. F.; Aparicio, L. M.; Rekoske, J. E.; Treviño, A. A. *The Microkinetics of Heterogeneous Catalysis*; American Chemical Society: Washington, DC, 1993.

(15) Grabow, L. C.; Gokhale, A. A.; Evans, S. T.; Dumesic, J. A.; Mavrikakis, M. *J. Phys. Chem. C* **2008**, *112*, 4608−4617.

(16) Kandoi, S.; Greeley, J.; Sanchez-Castillo, M. A.; Evans, S. T.; Gokhale, A. A.; Dumesic, J. A.; Mavrikakis, M. *Top. Catal.* **2006**, *37*, 17−28.

(17) Salciccioli, M.; Stamatakis, M.; Caratzoulas, S.; Vlachos, D. G. *Chem. Eng. Sci.* **2011**, *66*, 4319−4355.

(18) Hellman, A.; Honkala, K. *J. Chem. Phys.* **2007**, *127*, 194704.

(19) Lu, J.; Behtash, S.; Faheem, M.; Heyden, A. *J. Catal.* **2013**, *305*, 56−66.

(20) Chun, H.-J.; Apaja, V.; Clayborne, A.; Honkala, K.; Greeley, J. *ACS Catal.* **2017**, *7*, 3869−3882.
(21) Stamatakis, M.; Vlachos, D. G. *J. Chem. Phys.* **2011**, *134*, 214115.
(22) Stamatakis, M.; Vlachos, D. G. *ACS Catal.* **2012**, *2*, 2648−2663.
(23) Jansen, A. P. J. *An Introduction to Kinetic Monte Carlo Simulations of Surface Reactions (Lecture Notes in Physics)*; Springer-Verlag: Berlin and Heidelberg, Germany, 2012; Vol. *856*.
(24) Hansen, E. W.; Neurock, M. *Chem. Eng. Sci.* **1999**, *54*, 3411−3421.
(25) Mei, D.; Sheth, P. A.; Neurock, M.; Smith, C. M. *J. Catal.* **2006**, *242*, 1−15.
(26) Reuter, K. First-Principles Kinetic Monte Carlo Simulations for Heterogeneous Catalysis: Concepts, Status and Frontiers. In *Modeling Heterogeneous Catalytic Reactions: From the Molecular Process to the Technical System*; Deutschmann, O., Ed.; Wiley-VCH: Weinheim, Germany, 2012.
(27) Somorjai, G. A.; Li, Y. *Introduction to Surface Chemistry and Catalysis*; John Wiley & Sons, Inc.: New York, 1994.
(28) Evans, M. G.; Polanyi, M. *Trans. Faraday Soc.* **1935**, *31*, 875−894.
(29) van Eldik, R.; Asano, T.; le Noble, W. J. *Chem. Rev.* **1989**, *89*, 549−688.
(30) Grieger, R. A.; Eckert, C. A. *Trans. Faraday Soc.* **1970**, *66*, 2579−2584.
(31) Wong, K. F.; Eckert, C. A. *Trans. Faraday Soc.* **1970**, *66*, 2313−2319.
(32) Lawrance, G. A.; Stranks, D. R. *Acc. Chem. Res.* **1979**, *12*, 403−409.
(33) Klärner, F.-G.; Krawczyk, B.; Ruster, V.; Deiters, U. K. *J. Am. Chem. Soc.* **1994**, *116*, 7646−7657.
(34) Vannice, M. A. *J. Catal.* **1975**, *37*, 462−473.
(35) Dixit, R. S.; Tavlarides, L. L. *Ind. Eng. Chem. Process Des. Dev.* **1983**, *22*, 1−9.
(36) Winslow, P.; Bell, A. T. *J. Catal.* **1984**, *86*, 158−172.
(37) Cant, N. W.; Bell, A. T. *J. Catal.* **1982**, *73*, 257−271.
(38) Loveless, B. T.; Buda, C.; Neurock, M.; Iglesia, E. *J. Am. Chem. Soc.* **2013**, *135*, 6107−6121.
(39) Hibbitts, D. D.; Loveless, B. T.; Neurock, M.; Iglesia, E. *Angew. Chem., Int. Ed.* **2013**, *52*, 12273−12278.
(40) Hibbitts, D.; Dybeck, E.; Lawlor, T.; Neurock, M.; Iglesia, E. *J. Catal.* **2016**, *337*, 91−101.
(41) Dalla Betta, R. A.; Piken, A. G.; Shelef, M. *J. Catal.* **1974**, *35*, 54−60.
(42) Araki, M.; Ponec, V. *J. Catal.* **1976**, *44*, 439−448.
(43) van Herwijnen, T.; van Doesburg, H.; de Jong, W. A. *J. Catal.* **1973**, *28*, 391−402.
(44) Yates, I. C.; Satterfield, C. N. *Energy Fuels* **1991**, *5*, 168−173.
(45) Iglesia, E. *Appl. Catal., A* **1997**, *161*, 59−78.
(46) Ay, H.; Iglesia, E. unpublished work.
(47) Mims, C. A.; McCandlish, L. E. *J. Phys. Chem.* **1987**, *91*, 929−937.
(48) Ojeda, M.; Nabar, R.; Nilekar, A. U.; Ishikawa, A.; Mavrikakis, M.; Iglesia, E. *J. Catal.* **2010**, *272*, 287−297.
(49) Ojeda, M.; Li, A.; Nabar, R.; Nilekar, A. U.; Mavrikakis, M.; Iglesia, E. *J. Phys. Chem. C* **2010**, *114*, 19761−19770.
(50) Li, S.; Krishnamoorthy, S.; Li, A.; Meitzner, G. D.; Iglesia, E. *J. Catal.* **2002**, *206*, 202−217.
(51) Lohitharn, N.; Goodwin, J. G., Jr.; Lotero, E. *J. Catal.* **2008**, *255*, 104−113.
(52) den Breejen, J. P.; Radstake, P. B.; Bezemer, G. L.; Bitter, J. H.; Frøseth, V.; Holmen, A.; de Jong, K. P. *J. Am. Chem. Soc.* **2009**, *131*, 7197−7203.
(53) Carballo, J. M. G.; Yang, J.; Holmen, A.; García-Rodríguez, S.; Rojas, S.; Ojeda, M.; Fierro, J. L. G. *J. Catal.* **2011**, *284*, 102−108.
(54) Tuxen, A.; Carenco, S.; Chintapalli, M.; Chuang, C.-H.; Escudero, C.; Pach, E.; Jiang, P.; Borondics, F.; Beberwyck, B.; Alivisatos, A. P.; Thornton, G.; Pong, W.-F.; Guo, J.; Perez, R.; Besenbacher, F.; Salmeron, M. *J. Am. Chem. Soc.* **2013**, *135*, 2273−2278.
(55) Liuzzi, D.; Pérez-Alonso, F. J.; García-García, F. J.; Calle-Vallejo, F.; Fierro, J. L. G.; Rojas, S. *Catal. Sci. Technol.* **2016**, *6*, 6495−6503.
(56) Foppa, L.; Copéret, C.; Comas-Vives, A. *J. Am. Chem. Soc.* **2016**, *138*, 16655−16668.
(57) Petersen, M. A.; van den Berg, J.−A.; Ciobîcă, I. M.; van Helden, P. *ACS Catal.* **2017**, *7*, 1984−1992.
(58) Ge, Q.; Neurock, M. *J. Phys. Chem. B* **2006**, *110*, 15368−15380.
(59) Weststrate, C. J.; van Helden, P.; van de Loosdrecht, J.; Niemantsverdriet, J. W. *Surf. Sci.* **2016**, *648*, 60−66.
(60) Hibbitts, D.; Iglesia, E. *Acc. Chem. Res.* **2015**, *48*, 1254−1262.
(61) Escobar, M.; Gracia, F.; Karelovic, A.; Jiménez, R. *Catal. Sci. Technol.* **2015**, *5*, 4532−4541.
(62) Qi, Y.; Yang, J.; Duan, X.; Zhu, Y.-A.; Chen, D.; Holmen, A. *Catal. Sci. Technol.* **2014**, *4*, 3534−3543.
(63) Yang, J.; Qi, Y.; Zhu, J.; Zhu, Y.-A.; Chen, D.; Holmen, A. *J. Catal.* **2013**, *308*, 37−49.
(64) van Helden, P.; van den Berg, J.-A.; Ciobîcă, I. M. *Catal. Sci. Technol.* **2012**, *2*, 491−494.
(65) Liu, J.; Hibbitts, D. D.; Iglesia, E. unpublished results.
(66) Hibbitts, D. D.; Jiménez, R.; Yoshimura, M.; Weiss, B.; Iglesia, E. *J. Catal.* **2014**, *319*, 95−109.
(67) Hecker, W. C.; Bell, A. T. *J. Catal.* **1985**, *92*, 247−259.
(68) Chin, A. A.; Bell, A. T. *J. Phys. Chem.* **1983**, *87*, 3700−3706.
(69) Hecker, W. C.; Bell, A. T. *J. Catal.* **1983**, *84*, 200−215.
(70) Shangguan, J.; Olarte, M. V.; Chin, Y.-H. *J. Catal.* **2016**, *340*, 107−121.
(71) Braunchweig, B.; Hibbitts, D.; Neurock, M.; Wieckowski, A. *Catal. Today* **2013**, *202*, 197−209.
(72) Neurock, M.; Janik, M.; Wieckowski, A. *Faraday Discuss.* **2009**, *140*, 363−378.
(73) Koper, M. T. M.; Shubina, T. E.; van Santen, R. A. *J. Phys. Chem. B* **2002**, *106*, 686−692.
(74) Soled, S. L.; Malek, A.; Miseo, S.; Baumgartner, J.; Kliewer, C.; Afeworki, M.; Stevens, P. A. *Stud. Surf. Sci. Catal.* **2006**, *162*, 103−110.
(75) Dalla Betta, R. A. *J. Catal.* **1974**, *34*, 57−60.
(76) Shen, X.; Garces, L.-J.; Ding, Y.; Laubernds, K.; Zerger, R. P.; Aindow, M.; Neth, E. J.; Suib, S. L. *Appl. Catal., A* **2008**, *335*, 187−195.
(77) Yang, C.-H.; Goodwin, J. G., Jr. *J. Catal.* **1982**, *78*, 182−187.
(78) Bergeret, G.; Gallezot, P. In *Handbook of Heterogeneous Catalysis*; Ertl, G., Knözinger, H., Schüeth, F., Weitkamp, J., Eds.; Wiley-VCH Verlag GmbH & Co. KgaA: Weinheim, Germany, 2008, 738−765.
(79) Choi, M.; Wu, Z.; Iglesia, E. *J. Am. Chem. Soc.* **2010**, *132*, 9129−9137.
(80) Schneider, M.; Duff, D. G.; Mallat, T.; Wildberger, M.; Baiker, A. *J. Catal.* **1994**, *147*, 500−514.
(81) Koros, R. M.; Nowak, E. J. *Chem. Eng. Sci.* **1967**, *22*, 470.
(82) Wang, J.; Kispersky, V. F.; Delgass, W. N.; Ribeiro, F. H. *J. Catal.* **2012**, *289*, 171−178.
(83) Brauns, E. B.; Meier, R. J. *Vib. Spectrosc.* **2009**, *49*, 303−304.
(84) DeNoyer, L. K.; Dodd, J. G. In *Handbook of Vibrational Spectroscopy*; Chalmers, J. M., Griffiths, P. R., Eds.; John Wiley & Sons Ltd.: Chichester, UK, 2002; Vol. *3*.
(85) Kresse, G.; Hafner, J. *Phys. Rev. B: Condens. Matter Mater. Phys.* **1993**, *47*, 558−561.
(86) Kresse, G.; Hafner, J. *Phys. Rev. B: Condens. Matter Mater. Phys.* **1994**, *49*, 14251−14269.
(87) Kresse, G.; Furthmüller, J. *Phys. Rev. B: Condens. Matter Mater. Phys.* **1996**, *54*, 11169−11186.
(88) Kresse, G.; Furthmüller, J. *Comput. Mater. Sci.* **1996**, *6*, 15−50.
(89) Blöchl, P. E. *Phys. Rev. B: Condens. Matter Mater. Phys.* **1994**, *50*, 17953−17979.
(90) Kresse, G.; Joubert, D. *Phys. Rev. B: Condens. Matter Mater. Phys.* **1999**, *59*, 1758−1775.
(91) Perdew, J. P.; Burke, K.; Ernzerhof, M. *Phys. Rev. Lett.* **1996**, *77*, 3865−3868.
(92) Zhang, Y.; Yang, W. *Phys. Rev. Lett.* **1998**, *80*, 890.

DOI: 10.1021/jacs.7b04606
J. Am. Chem. Soc. 2017, 139, 11789−11802

(93) Hammer, B.; Hansen, L. B.; Nørskov, J. K. *Phys. Rev. B: Condens. Matter Mater. Phys.* **1999**, *59*, 7413−7421.
(94) Grimme, S.; Antony, J.; Ehrlich, S.; Krieg, H. *J. Chem. Phys.* **2010**, *132*, 154104.
(95) Grimme, S.; Ehrlich, S.; Goerigk, L. *J. Comput. Chem.* **2011**, *32*, 1456−1465.
(96) Monkhorst, H. J.; Pack, J. D. *Phys. Rev. B* **1976**, *13*, 5188−5192.
(97) Jónsson, H.; Mills, G.; Jacobsen, K. W. In *Classical and Quantum Dynamics in Condensed Phase Simulations*; Berne, B. J., Ciccotti, G., Coker, D. F., Eds.; World Scientific: New Jersey, London, 1998, 385−404.
(98) Henkelman, G.; Jónsson, H. *J. Chem. Phys.* **2000**, *113*, 9978−9985.
(99) Henkelman, G.; Jónsson, H. *J. Chem. Phys.* **1999**, *111*, 7010−7022.
(100) Groppo, E.; Bertarione, S.; Rotunno, F.; Agostini, G.; Scarano, D.; Pellegrini, R.; Leofanti, G.; Zecchina, A.; Lamberti, C. *J. Phys. Chem. C* **2007**, *111*, 7021−7028.
(101) Panagiotopoulou, P.; Kondarides, D. I.; Verykios, X. E. *J. Phys. Chem. C* **2011**, *115*, 1220−1230.
(102) Eckle, S.; Anfang, H.-G.; Behm, R. J. *J. Phys. Chem. C* **2011**, *115*, 1361−1367.
(103) Mojet, B. L.; Ebbesen, S. D.; Lefferts, L. *Chem. Soc. Rev.* **2010**, *39*, 4643−4655.
(104) Hoffmann, F. M. *Surf. Sci. Rep.* **1983**, *3*, 107−192.
(105) Bradshaw, A. M. *Surf. Sci.* **1978**, *72*, 513−535.
(106) Kale, M. J.; Christopher, P. *ACS Catal.* **2016**, *6*, 5599−5609.
(107) Heyden, B. E.; Bradshaw, A. M. *Surf. Sci.* **1983**, *125*, 787−802.
(108) Brandt, R. K.; Sorbello, R. S.; Greenler, R. G. *Surf. Sci.* **1992**, *271*, 605−615.
(109) Deshlahra, P.; Conway, J.; Wolf, E. E.; Schneider, W. F. *Langmuir* **2012**, *28*, 8408−8417.
(110) Hammaker, R. M.; Francis, S. A.; Eischens, R. P. *Spectrochim. Acta* **1965**, *21*, 1295−1309.
(111) Zaera, F. *Chem. Soc. Rev.* **2014**, *43*, 7624−7663.
(112) Meier, D. C.; Goodman, D. W. *J. Am. Chem. Soc.* **2004**, *126*, 1892−1899.
(113) Rainer, D. R.; Wu, M. C.; Mahon, D. I.; Goodman, D. W. *J. Vac. Sci. Technol., A* **1996**, *14*, 1184−1188.
(114) Oosterbeek, H. *Phys. Chem. Chem. Phys.* **2007**, *9*, 3570−3576.
(115) Dalla Betta, R. A.; Shelef, M. *J. Catal.* **1977**, *48*, 111−119.
(116) Krishnamoorthy, S.; Tu, M.; Ojeda, M. P.; Pinna, D.; Iglesia, E. *J. Catal.* **2002**, *211*, 422−433.
(117) Sato, K.; Inoue, Y.; Kojima, I.; Miyazaki, E.; Yasumori, I. *J. Chem. Soc., Faraday Trans. 1* **1984**, *80*, 841−850.
(118) Schlexer, P.; Pacchioni, G.; Włodarczyk, R.; Sauer, J. *Surf. Sci.* **2016**, *648*, 2−9.
(119) Abild-Pedersen, F.; Andersson, M. P. *Surf. Sci.* **2007**, *601*, 1747−1753.
(120) Fuggle, J. C.; Umbach, E.; Feulner, P.; Menzel, D. *Surf. Sci.* **1977**, *64*, 69−84.
(121) Pfnür, H.; Feulner, P.; Engelhardt, H. A.; Menzel, D. *Chem. Phys. Lett.* **1978**, *59*, 481−486.
(122) McEwen, J.-S.; Eichler, A. *J. Chem. Phys.* **2007**, *126*, 094701.
(123) Zhao, P.; He, Y.; Cao, D.; Wen, X.; Xiang, H.; Li, Y.-W.; Wang, J.; Jiao, H. *Phys. Chem. Chem. Phys.* **2015**, *17*, 19446−19456.
(124) Pfnür, H.; Menzel, D.; Hoffmann, F. M.; Ortega, A.; Bradshaw, A. M. *Surf. Sci.* **1980**, *93*, 431−452.
(125) Williams, E. D.; Weinberg, W. H. *Surf. Sci.* **1979**, *82*, 93−101.
(126) Pfnür, H.; Menzel, D. *J. Chem. Phys.* **1983**, *79*, 2400−2410.
(127) Biberrian, J. P.; van Hove, M. A. *Surf. Sci.* **1984**, *138*, 361−389.
(128) Starr, D. E.; Bluhm, H. *Surf. Sci.* **2013**, *608*, 241−248.
(129) Chen, Q.; Liu, J.; Zhou, X.; Shang, J.; Zhang, Y.; Shao, X.; Wang, Y.; Li, J.; Chen, W.; Xu, G.; Wu, K. *J. Phys. Chem. C* **2015**, *119*, 8626−8633.
(130) Eckert, C. A.; Boudart, M. *Chem. Eng. Sci.* **1963**, *18*, 50.
(131) Khotimah, S. N.; Viridi, S. *J. Pengajaran Fis. Sekol. Menengah* **2010**, *2*, 15−18.
(132) Bondi, A. *J. Phys. Chem.* **1964**, *68*, 441−51.
(133) Landry, S. M.; Dalla Betta, R. A.; Lü, J. P.; Boudart, M. *J. Phys. Chem.* **1990**, *94*, 1203−1206.
(134) Kieken, L.; Boudart, M. *Catal. Lett.* **1993**, *17*, 1−10.

DOI: 10.1021/jacs.7b04606
J. Am. Chem. Soc. 2017, 139, 11789−11802